

Outflow – Core Interaction in Barnard 1

Masaaki Hiramatsu^{1,2}, Naomi Hirano¹, and Shigehisa Takakuwa¹

ABSTRACT

In order to study how outflows from protostars influence the physical and chemical conditions of the parent molecular cloud, we have observed Barnard 1 (B1) main core, which harbors four Class 0 and three Class I sources, in the CO ($J = 1 - 0$), CH₃OH ($J_K = 2_K - 1_K$), and the SiO ($J = 1 - 0$) lines using the Nobeyama 45 m telescope. We have identified three CO outflows in this region; one is an elongated (~ 0.3 pc) bipolar outflow from a Class 0 protostar B1-c in the submillimeter clump SMM 2, another is a rather compact (~ 0.1 pc) outflow from a Class I protostar B1 IRS in the clump SMM 6, and the other is an extended outflow from a Class I protostar in SMM 11. In the western lobe of the SMM 2 outflow, both the SiO and CH₃OH lines show broad redshifted wings with the terminal velocities of 25 km s^{-1} and 13 km s^{-1} , respectively. It is likely that the shocks caused by the interaction between the outflow and ambient gas enhance the abundance of SiO and CH₃OH in the gas phase. The total energy input rate by the outflows ($1.1 \times 10^{-3} L_{\odot}$) is smaller than the energy loss rate ($8.5 \times 10^{-3} L_{\odot}$) through the turbulence decay in B1 main core, which suggests that the outflows can not sustain the turbulence in this region. Since the outflows are energetic enough to compensate the dissipating turbulence energy in the neighboring, more evolved star forming region NGC 1333, we suggest that the turbulence energy balance depends on the evolutionary state of the star formation in molecular clouds.

Subject headings: stars: formation — stars: low mass — stars: pre-main sequence — ISM: clouds — ISM: jets and outflows — ISM: individual (Barnard 1)

1. INTRODUCTION

Molecular outflows are common features accompanied with young stellar objects (YSOs; Bachiller 1996). The outflows have large impacts on the surrounding molecular cloud both in

¹Academia Sinica Institute of Astronomy and Astrophysics, P.O. Box 23-141, Taipei 10617, Taiwan; hiramatsu@asiaa.sinica.edu.tw

²Institute of Astronomy, National Tsing Hua University, Hsinchu 33302, Taiwan

the chemical and physical aspect. Shocks excited by the propagation of the outflow raise the temperature of surrounding material and liberate various molecules such as NH_3 , CH_3OH and SiO from dust grains (Allamandola et al. 1992; Schilke et al. 1997; Bachiller et al. 2001; Jørgensen et al. 2004). As a result, the relative abundance of these molecules against H_2 reaches several orders of magnitude larger than that in quiescent molecular clouds.

The supersonic turbulence in molecular clouds is ubiquitous but should quickly dissipate through shocks, thus some driving sources are needed (Mac Low et al. 1998). Protostellar outflows are considered to be possible sources to maintain the supersonic turbulence in molecular clouds (Norman & Silk 1980) and regulate the star formation, since the turbulence serves as a counterwork against the gravitational collapse in molecular clouds. The observational studies of Herbig-Haro (HH) objects (Walawender et al. 2005a) and CO outflows (Knee & Sandell 2000; Stanke & Williams 2007) compared the energy input by the outflows and turbulence energy decay, and found that the outflows have enough energy to retain the turbulence in the molecular clouds in at least local scale (~ 0.5 pc), such as NGC 1333 or L1641-N, but not whole Perseus or Orion giant molecular cloud scale ($\gtrsim 10$ pc). The theoretical simulation also pointed out that the protostellar outflows play an important role to retain the turbulence and regulate the star formation efficiency (Li & Nakamura 2006).

Barnard 1 (B1) is one of the star-forming regions located in the Perseus molecular cloud complex. The distance to B1 is estimated to be 230 pc by Černis & Straizys (2003) on the basis of the extinction study. This value is consistent with the distance of 235 ± 15 pc to the NGC 1333 molecular cloud, which is located at $\sim 1^\circ$ west of B1, derived from the parallax measurements of the H_2O masers associated with the YSO SVS 13 (Hirota et al. 2008). Note that this distance is different from the previously adopted values of 350 pc and 318 pc, which are the distances to the Perseus OB2 association (Borgman & Blaauw 1964; de Zeeuw et al. 1999). B1 was observed in several molecular lines by Bachiller et al. (1990). They revealed that the dense part of the cloud traced by the C^{18}O (1 – 0) line has a size of $\sim 1.3 \times 3.5$ pc and a mass of $518 M_\odot$. Inside this region, a denser portion called “main core” with a diameter of 0.5 pc and a mass of $65 M_\odot$ ¹ was found in the NH_3 emission. A submillimeter continuum survey (Walawender et al. 2005b) identified 12 submillimeter clumps in B1 and six of them are located in the main core region. Two of the submillimeter clumps (SMM 1 and SMM 2) harbor Class 0 YSOs and one (SMM 6) harbors a Class I YSO. Inside SMM 1, there are two extremely young sources, B1-bN and B1-bS (Hirano et al. 1999). A Class I source in SMM 6 was detected by *IRAS* and is referred as IRAS 03301+3057 or B1 IRS, and accompanied by an outflow (Bachiller et al. 1990; Yamamoto et al. 1992; Hirano et al. 1997;

¹These values are corrected for the difference of the assumed distance from 350 pc to 230 pc.

de Gregorio-Monsalvo et al. 2005). The YSO in SMM 2 (also referred as B1-c) located at $\sim 1'$ north of IRAS 03301+3057 is also a driving source of the outflow that is extending along the east-west direction. In addition to those four YSOs (B1 IRS, B1-bN, B1-bS, and B1-c), one Class 0 YSO was identified in SMM 3, and one Class I source in SMM 11 (Hatchell et al. 2007a). There is another Class I source, LkH α 327, without any submillimeter counterpart. In total, four Class 0 and three Class I sources are identified in B1 main core. The properties of the YSOs in B1 main core are summarized in Table 1. Near infrared observations in H α and H $_2$ rovibrational lines found a number of shocks produced by protostellar outflows in the B1 main core region (Walawender et al. 2005a,b, 2009). The most prominent shocks are associated with the outflow from SMM 2. Mid-infrared observations with *Spitzer Space Telescope* have clearly revealed the S-shaped features of the knotty chains of the shocks centered at SMM 2, as well as several shocked regions around SMM 1, SMM 6, and SMM 11 (Jørgensen et al. 2006).

This paper presents multi-molecular line observations of B1 main core to investigate the effects of protostellar outflows on the physical and chemical properties of the surrounding core. The details of our observations are described in Section 2. The results of the observations in CO, CH $_3$ OH, and SiO lines are described in Section 3, followed by the discussion on the chemical abundance of the molecules and turbulence energy budget in Section 4 and a summary in Section 5.

2. OBSERVATIONS

CO ($J = 1 - 0$), CH $_3$ OH ($J_K = 2_K - 1_K$), and SiO ($J = 1 - 0$) line observations were performed in 2006 April with the 45 m telescope at Nobeyama Radio Observatory (NRO). The frequencies of the observed lines are summarized in Table 2. The 25-Beam Array Receiver System (BEARS; Sunada et al. 2000) operated in the double sideband (DSB) mode was used for the CO and CH $_3$ OH observations. The system noise temperature of BEARS during the observations was in the range of T_{sys} (DSB) = 200 – 500 K. The main beam efficiency was $\eta_{\text{MB}} \sim 0.45$ at 115 GHz. The half power beamwidth (HPBW) was 18'' at 97 GHz (CH $_3$ OH) and 15'' at 115 GHz (CO), and the separation between each beam was 41'.1. Twelve pointings of BEARS were adopted to map the 10' \times 6'.5 region, which covers the entire region of B1 main core, with a grid spacing of 29'.1. The intensity scales of the 25 receiver beams of BEARS at 97 GHz were calibrated by comparing the intensity of NGC 2264 observed by each beam of BEARS with that measured by the single-beam receiver S100. The intensity scales of the 25 beams at 115 GHz were calibrated using the scaling factor table provided by the observatory. The back end was an autocorrelator with a bandwidth of 32

MHz and a frequency resolution of 37.8 kHz, which corresponds to a velocity resolution of 0.098 km s^{-1} and 0.12 km s^{-1} at 115 GHz (CO) and 97 GHz (CH₃OH), respectively.

The SiO ($J = 1 - 0$) line was observed along the jets from SMM 2 and SMM 6 with a single-beam SIS receiver S40 operated in the single-sideband (SSB) mode. The position angles of the strip scans are 77° and 133° for SMM 2 and SMM 6, respectively. The observational grid spacing was $38''.4$, which was the same as the HPBW at 43 GHz. The system noise temperature T_{sys} (SSB) during the observations was $\sim 180 - 300 \text{ K}$. The main beam efficiency was $\eta_{\text{MB}} = 0.77$ at 43 GHz. The bandwidth of the autocorrelator was set to 32 MHz. The spectral resolution was 37.8 kHz which corresponds to a velocity resolution of 0.26 km s^{-1} at 43 GHz.

The telescope pointing was checked by observing the SiO maser emission from NML Tau every 60-90 minutes and the error was estimated to be less than $\sim 6''$ in 100 GHz and $10''$ in 43 GHz observations. The standard chopper-wheel method (Kutner & Ulich 1981) was adopted to convert the received signal into the antenna temperature. The data were reduced using NEWSTAR, a data reduction software developed by NRO. Linear baselines were subtracted in most cases.

3. RESULTS

3.1. Molecular Outflow Traced by the CO Line

3.1.1. Distribution of the Outflows

Figure 1 displays the CO ($1 - 0$) line profiles observed at four representative positions in B1 main core, i.e. (a) $120''$ west of SMM 2, (b) SMM 6, (c) SMM 1, and (d) $5'.5$ southwest of SMM 6. In this paper, these four positions are referred to as positions “a”, “b”, “c”, and “d”, respectively. Since there is no jet-like component around this position in the infrared image (Walawender et al. 2005b), it is likely that the spectrum observed at the position d is not affected by outflows. Therefore, the velocity range of the ambient cloud component, “line core”, was determined to be from $V_{\text{LSR}} = 2.1 \text{ km s}^{-1}$ to $V_{\text{LSR}} = 9.6 \text{ km s}^{-1}$, using the CO spectrum at the position “d”. The CO emission outside of this velocity range is regarded as the outflow component. The CO spectra obtained at the positions “a” and “b” exhibit line wings in the redshifted side and blueshifted side, respectively. The most prominent CO redshifted wing was observed at the position “a”. At the position “c”, wing-like blueshifted emission is detected in the velocity range of $1 \text{ km s}^{-1} < V_{\text{LSR}} < 3 \text{ km s}^{-1}$. This component might be originated from an outflow associated with SMM 1, however, because of its low

velocity, it is unclear whether this component arises from the outflow or not. In addition, the spatial distribution of the blueshifted CO wing (see below) is not localized on SMM 1. Therefore, in this paper we do not include this component as an outflow candidate.

The spatial distributions of the blue- and redshifted outflow components are shown in Fig.2. Although the spatial distributions of the high velocity components are complex, two bipolar outflows centered at SMM 2 and SMM 6, and the extended blueshifted emission at the southeast corner are recognized. The outflow centered at SMM 2 extends along the east–west direction. The extent of the westward redshifted component is $120''$ (0.13 pc) and reaches the position of a shocked region MH 2 (Walawender et al. 2005b). The redshifted emission peaks at the head of the lobe (position “a”) and the velocity is also the largest at this position. On the other hand, the eastern blueshifted component peaks at $150''$ (0.17 pc) southeast of SMM 2. Neither the redshifted peak in the west nor the blueshifted peak in the east was covered by the previous CO (3 – 2) map (Hatchell et al. 2007b) and the interferometric CO (1 – 0) map (Matthews et al. 2006). Hence the entire picture of this outflow has been revealed by our observations for the first time. There is a compact blueshifted component in the western lobe and an extended redshifted component in the eastern lobe. This suggests that the outflow axis is close to the plane of the sky, and the overlapping blueshifted and redshifted components are due to the projection of the front and back sides of the lobes. The outflow traced by the CO line is well aligned with the S-shaped knots seen in the *Spitzer* IRAC band 2 image (Jørgensen et al. 2006). This IRAC band contains several H₂ pure-rotational lines that are considered to arise from shocked regions. Therefore, it is likely that the S-shaped feature traces the shocks in the outflow driven by SMM 2.

The outflow from SMM 6 is more compact than that from SMM 2. The blueshifted emission is detected toward the position of SMM 6 and slightly extended ($\sim 40''$, 0.04 pc) to the northeast. There is a redshifted component which peaks at $65''$ (0.07 pc) southwest of SMM 6. It is uncertain whether this redshifted component is originated from the SMM 6 outflow or not, because there is another YSO candidate SSTc2d J033314.4+310711 at $20''$ (0.02 pc) east of the redshifted peak. This source is classified as a “YSOc_red” (YSO candidate and red) in the *Spitzer* c2d catalog, and might be the driving source of the redshifted outflow. However, the grid spacing of the current observations is not fine enough to pinpoint the position of the driving source unambiguously. Therefore, in the following discussion, the redshifted component at $65''$ southwest of SMM 6 is treated as a redshifted lobe of the SMM 6 outflow. A series of shocked knots MH 4 was found at $15''$ west of SMM 6 and thought to be emanated from SMM 6 (Walawender et al. 2005b, 2009). These knots align east–west direction and are not parallel to the SMM 6 CO outflow. Since the length of the knots is $20''$, smaller than our mapping grid spacing, the relation between the knots and the SMM 6 outflow is not clear in the present observations. An elongated reflection nebula was identi-

fied in the K_s -band image around SMM 6 (Walawender et al. 2005b) and the orientation is consistent with that of the SMM 6 outflow. This consistency would support the idea that SMM 6 is the driving source of the redshifted component southwest of SMM 6.

The extended blueshifted CO emission is found around the shocked knots MH 8 and HH 790. In the CO image, this blueshifted component is continuously connected to the blueshifted lobe of the SMM 2 outflow. If this blueshifted component in the southeast area is a part of the SMM 2 outflow, however, the outflow is highly asymmetric with a blueshifted lobe more than twice as longer as the redshifted lobe. In addition, the blueshifted lobe bends sharply to the south at the position around the MH 1 knot. In contrast, the shocked components seen in the *Spitzer* image suggest that the eastern lobe and the western lobe of the SMM 2 outflow are similar in length. Therefore, it is possible that the blueshifted emission in the southeastern area originates from the other outflow. One possible candidate is the giant east–west outflow from SMM 11, which was identified in the deep H_2 image obtained by Walawender et al. (2009). This outflow is parallel to the SMM 2 outflow, and contains MH 8 and HH 790 in the eastern lobe. If MH 8 and HH 790 are related to the outflow from SMM 11, it is natural to consider that the blueshifted CO component around MH 8 and HH 790 is also a part of the SMM 11 outflow. In the H_2 image, the western lobe of the SMM 11 outflow extends to MH 10 and MH 3. The redshifted CO emission was detected around MH 10 and would be the part of the SMM 11 outflow. However, the giant outflow extending further west was not clearly detected in our CO observations.

The outflows from SMM 1, SMM 3, and LkH α 327 are not clearly seen in our CO (1–0) map, although they were reported by Hatchell et al. (2007b) on the basis of the CO (3–2) observations, except for that from LkH α 327. Our CO (1–0) maps show the redshifted emission to the northeast of SMM 1. This component is also seen in the CO (3–2) map of Hatchell et al. (2007b), and identified as the redshifted lobe of the SMM 1 outflow. It is possible that this redshifted emission is related to the outflow from SMM 1 as argued by Hatchell et al. (2007b). However, we regard this emission as a part of the outflow from SMM 11 because there is no clear blueshifted component and bipolarity around SMM 1. The mid- and near infrared images show a chain of shocked knots that extends from SMM 1 to SMM 3. The axis of this knot complex is parallel to that of the SMM 6 outflow. Although SMM 1 is designated to be a driving source of these shocked features (Walawender et al. 2009), no corresponding CO high-velocity component was detected in the present observations. LkH α 327 was classified as Class I based on the spectral energy distribution slope in the *IRAS* 12–100 μm data (Walawender et al. 2005b). On the other hand, this source was classified as Class II based on the Two Micron All Sky Survey K -band, *Spitzer* IRAC, and MIPS data. The facts that LkH α 327 is located at the periphery of B1 main core and not associated with any 850 μm emission indicate that the source is in the rather evolved stage.

3.1.2. Estimation of the Kinematic Properties of the Outflows

The mass, momentum, kinetic energy, and the momentum flux of the identified CO outflows are calculated with the method described by Bourke et al. (1997). In this procedure, we divided the high-velocity CO emissions originated from the outflows into the 0.4 km s^{-1} velocity bins, and calculated the quantities on an assumption of the local thermal equilibrium (LTE) condition. First, the column density of the molecule in the velocity range of v to $v + \Delta v$, $N(v)$, is given as

$$N(v) = \frac{3hZ(T)}{8\pi^3\mu^2(J+1)} \frac{\exp\{hBJ(J+1)/kT_{\text{ex}}\}}{1 - \exp(-h\nu/kT_{\text{ex}})} f \int_v^{v+\Delta v} \tau dv, \quad (1)$$

where

$$f = \frac{T_{\text{MB}}}{J(T_{\text{ex}}) - J(T_{\text{bg}})} \frac{1}{1 - \exp(-\tau)}, \quad (2)$$

$$J(T) = \frac{h\nu/k}{\exp(h\nu/kT) - 1}, \quad (3)$$

h is the Planck constant, $Z(T)$ is the partition function, μ is the dipole moment of the molecule, B is the rotation constant of the molecule, k is the Boltzmann constant, ν is the frequency of the line, τ is the optical depth, T_{ex} is the excitation temperature, and T_{bg} is the background temperature. For linear molecules such as CO, the partition function is approximated to be $Z(T) = kT/hB$ if $hB \ll kT$. In the case of the CO (1 – 0) line under the optically thin assumption, the above equations become the following as given by Bourke et al. (1997):

$$N(v) = 2.31 \times 10^{14} \frac{T_{\text{ex}} + 0.92}{1 - \exp(-5.53/T_{\text{ex}})} \frac{1}{J(T_{\text{ex}}) - J(T_{\text{bg}})} \int_v^{v+\Delta v} T_{\text{MB}} dv. \quad (4)$$

The mass at each observed position (α, δ) and velocity v , $M(v, \alpha, \delta)$ is given as

$$M(v, \alpha, \delta) = [\text{H}_2/\text{CO}] \mu_{\text{m}} m_{\text{H}} A(\alpha, \delta) N(v), \quad (5)$$

where $[\text{H}_2/\text{CO}]$ is the reciprocal of the CO abundance and adopted to be 10^4 , $\mu_{\text{m}} = 2.72$ is the mean molecular mass per H_2 , m_{H} is the mass of a hydrogen atom, and $A(\alpha, \delta)$ is the area of the CO emission at a given observed position. Since the observing grid spacing ($29''.1$) is larger than the telescope beam ($15''$), we adopted the squared value of the observing grid spacing as $A(\alpha, \delta)$ under the assumption of the uniform emission distribution in the $29''.1^2$ region. The mass at each velocity bin $M(v)$ is estimated by integrating $M(v, \alpha, \delta)$ over the outflow spatial extension, and then the total mass is derived by integrating $M(v)$ over the outflow velocity range.

Since the optical depth of the CO line is not obtained in our observations, the assumption of the optically thin CO (1–0) line is adopted, hence the estimation should be a lower limit. The excitation temperature T_{ex} is estimated by comparing the CO (1–0) spectra and (3–2) spectra (Hatchell et al. 2007b) as follows. Under the LTE condition, the total column density N and the column density at a given rotational energy level J , N_J , is given as

$$N = N_J \frac{Z}{2J+1} \exp\{hBJ(J+1)/kT_{\text{ex}}\}. \quad (6)$$

N_J is also expressed as

$$N_J = \frac{8\pi\nu^3}{c^3} \frac{2J+1}{(2J+3)A_{J+1,J}} \frac{1}{1 - \exp(-h\nu/kT_{\text{ex}})} \int T_{\text{MB}} dv \quad (7)$$

in the optically thin condition, where $A_{J+1,J}$ is the Einstein A coefficient for the transition from the level $J+1$ to J . The relation between the excitation temperature T_{ex} and the line intensity ratio of the CO (3–2) and (1–0) transition is derived from Equations (6) and (7):

$$\frac{\int T_{\text{MB},3-2} dv}{\int T_{\text{MB},1-0} dv} = 3 \exp(-16.6/T_{\text{ex}}) \frac{1 - \exp(-16.6/T_{\text{ex}})}{1 - \exp(-5.53/T_{\text{ex}})} \quad (8)$$

The integrated intensities of the high-velocity CO (3–2) line toward the SMM 2 westward redshifted component and SMM 6 were calculated from the spectra shown by Hatchell et al. (2007b). The integrated intensities, line ratios and the derived excitation temperatures are summarized in Table 3. Although the observed positions in the two transitions are slightly different, the offset ($< 5''$) is smaller than 1/3 of the beam size and we ignore the positional difference. The derived excitation temperatures toward the two positions, 46 K and 42 K, are close to each other. We note that the derivation of the excitation temperature is sensitive to the accuracy of the relative calibration between the two independent observations with the different instruments. For example, a 20% uncertainty of the ratio yields ± 20 K uncertainty of the excitation temperature. Here we adopt 50 K as a value of the excitation temperature for the calculations of the outflow parameters. This value is the same as that used by Hatchell et al. (2007b) to calculate the outflow properties in the Perseus molecular cloud.

The momentum P , kinetic energy E_k , dynamical timescale t_d , and the outflow momentum flux F_{outflow} are described as

$$P = \int M(v)(v - v_0) dv, \quad (9)$$

$$E_k = \frac{1}{2} \int M(v)(v - v_0)^2 dv, \quad (10)$$

$$t_d = R/v_{\text{ch}} = R/(P/M), \quad (11)$$

$$F_{\text{outflow}} = P/t_d, \quad (12)$$

where v_0 is the systemic velocity of 6.7, 6.5, and 6.8 km s⁻¹ for the SMM 2, SMM 6, and SMM 11 outflows, respectively, measured by fitting a Gaussian function to the CH₃OH spectra toward the sources (see Section 3.2). R is the length of the outflow and $v_{\text{ch}} = P/M$ is the characteristic velocity. The mass-loss rate is estimated as $\dot{M} = F_{\text{outflow}}/v_{\text{wind}}$, where v_{wind} is the velocity of the primary wind ejected from the close vicinity of the protostar. Since we do not have any information on the wind velocity from our observations, we assume $v_{\text{wind}} = 100$ km s⁻¹ (e.g., Giovanardi et al. 1992).

The inclination angle of the outflow axis is also unclear, therefore we employed 57:3 from the line of sight, which is the mean inclination angle on the assumption of the random outflow orientation. This assumption should be reasonable for the SMM 2 outflow because the interferometric observations revealed that the opening angle of the outflow cavity in the 20'' scale is $\sim 55^\circ$ and the red and blueshifted lobes are not overlapped at the position of the driving source (Matthews et al. 2006), which indicates that the outflow axis inclines at the larger angle than the opening angle. This interpretation does not conflict with the fact that the blue- and redshifted components are overlapped in the larger scale as shown in Fig.2, because these overlapped blue- and redshifted components are interpreted as the cavity wall. For the SMM 6 outflow, Hirano et al. (1997) suggested that the configuration of the SMM 6 outflow is in a pole-on geometry, while de Gregorio-Monsalvo et al. (2005) suggested that the outflow from SMM 6 is inclined toward southwest. Since it is difficult to estimate the inclination angle from our coarse grid observations and there is no consensus on the inclination angle of the SMM 6 outflow, it is reasonable to adopt the mean inclination angle. Since there is no previous study about the inclination angle for the SMM 11 outflow, we also adopt the mean inclination angle of 57:3.

The blueshifted lobes of the outflows from SMM 2 and SMM 11 are not clearly separated in our observations. Therefore, we assumed that the transverse extent of the SMM 2 outflow lobe is symmetric with respect to the shocked knots, and regarded the blueshifted component at decl. $> 31^\circ 08'$ as the SMM 2 outflow and that at decl. $< 31^\circ 08'$ as the SMM 11 outflow. The redshifted lobe of the SMM 11 outflow is also confused with the eastern redshifted component of the SMM 2 outflow. We assumed that the northeastern half of the redshifted component at the east of SMM2 belongs to the SMM 2 outflow, because this part is overlapped with the blueshifted lobe of the SMM 2 outflow. The southwestern half of this redshifted component is regarded as the redshifted lobe of the SMM 11 outflow. The outflow parameters derived on the above assumptions are summarized in Table 4.

The mass, momentum, and kinetic energy of the SMM 2 outflow are almost comparable to those of the SMM 11 outflow and a factor of 5–10 larger than those of the SMM 6 outflow. The properties of outflows from Class 0 and Class I sources were compiled by Bontemps et al.

(1996), and it was found that the outflow momentum flux is 1 order of magnitude larger for Class 0 sources. The mean momentum flux is $\langle F_{\text{CO}} \rangle = 5.7 \times 10^{-5} M_{\odot} \text{ km s}^{-1} \text{ yr}^{-1}$ and $3.8 \times 10^{-6} M_{\odot} \text{ km s}^{-1} \text{ yr}^{-1}$ for Class 0 and Class I sources, respectively (Bontemps et al. 1996). Considering that they adopted an opacity correction of a factor of 3.5, the momentum fluxes of the outflows emanated from SMM 2 and SMM 6 are in reasonable agreement with the mean values for Class 0 and I sources, respectively. On the other hand, the outflow from SMM 11 has approximately 1 order of magnitude larger momentum flux compared to the mean value of the outflows from the Class I sources, probably because the spatial extent of this outflow is large.

The momentum fluxes for the outflows were estimated by Hatchell et al. (2007b) based on their CO (3 – 2) observations. Converting the assumed distance to B1 from 320 pc to 230 pc, the momentum fluxes are $F_{\text{CO}} = 1.2 \times 10^{-7}$, 9.1×10^{-7} , and $3.2 \times 10^{-7} M_{\odot} \text{ km s}^{-1} \text{ yr}^{-1}$ for the SMM 2, SMM 6, and SMM 11 outflow, respectively. The momentum flux they derived for all the outflows is smaller than our result, and the difference reaches a factor of 70 for the SMM 2 outflow. There are several reasons for these discrepancies. First, they did not take the correction of the inclination i into account, and this correction makes the momentum flux larger by a factor of $\sin i / \cos^2 i$ (Bontemps et al. 1996). Our assumption of the inclination of $57^{\circ}3$ yields the factor of 2.9. Second, we regard both the westward and eastward redshifted components as the outflow from SMM 2, however, Hatchell et al. (2007b) assigned the eastward redshifted component to the SMM 1 (B1-bS) outflow. This different identification causes another factor of 2 discrepancy in the estimation of the outflow momentum flux. Finally, the mapped region by Hatchell et al. (2007b) does not cover the entire extent of the outflow from SMM 2. In general, the outflow momentum flux is a robust parameter against incomplete mappings. If a considerable fraction of the total momentum is carried by components outside the mapping area, however, incomplete mapping observations might result in underestimation of the momentum flux. In fact, the prominent redshifted component around the position “a” is located outside of the mapped area by Hatchell et al. (2007b).

3.2. CH₃OH

The CH₃OH line profiles at three representative positions, i.e. (a) 120'' west of SMM 2, (b) SMM 6, and (c) SMM 1, are displayed in Fig. 3. The frequency separations between the $2_0 - 1_0 A^+$ and the $2_{-1} - 1_{-1} E$ lines and the $2_0 - 1_0 E$ and the $2_0 - 1_0 A^+$ lines correspond to 9.8 km s^{-1} and 6.3 km s^{-1} , respectively. The widest line profile is seen at the position “a” (Fig.3a) where the peak of the CO redshifted outflow is located. At this position, the

$2_0 - 1_0 A^+$ and $2_{-1} - 1_{-1} E$ lines are blended because of the broad redshifted wings. The terminal velocity of the $2_{-1} - 1_{-1} E$ line reaches 13 km s^{-1} away from the systemic velocity. The position “a” is located close ($\sim 10''$) to the branching point of the shocked feature seen in the *Spitzer* image (see Fig.2). Similar blended CH_3OH profiles are seen in three observed points around the position “a”. Toward SMM 6, both the $2_0 - 1_0 A^+$ and $2_{-1} - 1_{-1} E$ lines show a blueshifted wing (Fig.3b) which is also seen in the CO line (Fig.1b). No wing components are detected toward SMM 1(Fig.3c) where no CO outflow was identified. From these results we divide the CH_3OH emission into three velocity ranges; the blueshifted component ($V_{\text{LSR}} < 5.5 \text{ km s}^{-1}$), the line core component ($5.5 \text{ km s}^{-1} < V_{\text{LSR}} < 7.5 \text{ km s}^{-1}$), and the redshifted component ($V_{\text{LSR}} > 7.5 \text{ km s}^{-1}$).

The integrated intensity maps of the CH_3OH lines are shown in Fig.4. Since the distribution of the $2_0 - 1_0 A^+$ line is similar to that of the $2_{-1} - 1_{-1} E$ line, and these two lines are blended around the position “a”, we integrated all the $2_0 - 1_0 A^+$ and $2_{-1} - 1_{-1} E$ emission over the velocity of $-3.6 \text{ km s}^{-1} < V_{\text{LSR}} < 20.4 \text{ km s}^{-1}$ with the reference frequency of 96.73939 GHz , the rest frequency of $2_{-1} - 1_{-1} E$ line, and made a combined map which is shown in Fig.4. Hereafter we call this map “ $A + E$ map”. The CH_3OH ($J_K = 2_0 - 1_0 A^+$, $2_{-1} - 1_{-1} E$) lines were detected around the dusty clump complex which contains SMM 1, SMM 2, SMM 3, and SMM 6. There are two peaks seen in the $A + E$ map; one peak is located at the position “a” and the other peak is located around SMM 6. No obvious peaks are detected in the eastern side of the SMM 2 outflow and around the other protostars. The observed CH_3OH distribution is different from those of the dust continuum and NH_3 emission (Matthews & Wilson 2002; Walawender et al. 2005b; Bachiller et al. 1990). Since one CH_3OH peak located at the position “a” coincides with the peak of the redshifted CO emission, we examined the contribution of the high-velocity component to the $A + E$ map by comparing the spatial distributions of the blue- and redshifted CH_3OH emission with that of the line core emission (Fig. 5). The high-velocity components peak at the position “a” and SMM 6, and it is obvious that the $A + E$ map is largely affected by the high-velocity components. The line core emission shows a single peak at SMM 6, and its distribution is different from the distribution of the NH_3 emission which peaks around SMM 1. The distribution of the CH_3OH line core emission is also different from the distribution of the dust continuum emission which peaks at the positions of the SMM sources (Walawender et al. 2005b). The coincidence of the peaks of the line core component and the high velocity (blueshifted) component at SMM 6 indicates that the peak around SMM 6 seen in the $A + E$ map arises from both the quiescent gas and the outflow-related component. The CH_3OH abundance enhancement due to the outflow – core interaction is a possible reason for the intensity enhancement around the outflows. The abundance enhancement is discussed in Section 4.1.

The CH₃OH 2₀ – 1₀ *E* transition is much weaker than the other two transitions and detected above the 3σ noise level at eight out of the 300 observed positions. An example of the spectrum is shown in Fig.3c, which is detected at (α, δ)(J2000)=(3^h33^m20^s.8, 31°07′25″.1), 10″ southwest of the Class 0 protostar SMM 1 (B1-bS). The integrated intensity map of the 2₀ – 1₀ *E* transition is shown in Fig.4 with red contours. This line shows its intensity peak around SMM 1 and extension to SMM 2 and 6. The CH₃OH 2₀ – 1₀ *E* emission peak at SMM 1 is not seen in the other two transitions, whereas the high density tracers such as the NH₃ (1,1), H¹³CO⁺ (*J* = 1 – 0) lines, and 850 μm continuum emission show the emission peaks around SMM 1 (Bachiller et al. 1990; Hirano et al. 1999; Matthews & Wilson 2002). The upper state energy of the 2₀ – 1₀ *E* transition is 12.2 K, which is slightly higher than those of the other two transitions, 4.6 and 7.0 K for the 2₋₁ – 1₋₁ *E* and 2₀ – 1₀ *A*⁺ transition, respectively (obtained from CDMS catalog, Muller et al. 2001). Since CH₃OH emission tends to be sub-thermally excited in star-forming regions (Buckle & Fuller 2002), the difference of the distributions between the 2₀ – 1₀ *E* transition and the other lower-excitation transitions is likely to reflect the density structure of B1 main core, as the 2₀ – 1₀ *E* line and the high-density tracers show the common peak at SMM 1.

3.3. SiO Emission along the Outflows

The SiO (*J* = 1 – 0) emission was detected at four positions out of 13 observed positions along the SMM 2 outflow (Fig.6). The line profiles at the representative positions are shown in Fig.7. In the northwestern lobe of the SMM 2 outflow, the SiO emission is redshifted and its line width increases as the distance from SMM 2 increases (from SMM 2 W1 to SMM 2 W3, see Fig.6). The terminal velocity of the SiO emission reaches up to 25 km s⁻¹ at the position of SMM 2 W3, which corresponds to the peak of the redshifted CO emission. In the southeastern lobe, the SiO emission was detected only at one position labeled SMM 2E. This position corresponds to the peak of the blueshifted CO emission. However, the SiO emission peaks at *V*_{LSR} = 7.7 km s⁻¹, which is redshifted with respect to the cloud systemic velocity. At the position of SMM 2 itself, there was no detectable SiO emission.

The SiO emission originated from the SMM 6 outflow was searched for at four positions along the outflow, and the emission was detected only at the position of SMM 6. As shown in Fig.7, the SiO line at SMM 6 shows the narrow component ($\Delta V = 1.3$ km s⁻¹) with its peak velocity at the systemic velocity of *V*_{LSR} = 6.4 km s⁻¹, and a possible blueshifted component with the terminal velocity of ~ 5 km s⁻¹ with respect to the systemic velocity. Yamamoto et al. (1992) also reported the detection of the SiO *J* = 1 – 0 and 2 – 1 emission lines at 7″ northwest from the position of SMM 6. They pointed out that the line profile

consists of a narrow ($\Delta v = 1.6 \text{ km s}^{-1}$) component and broad ($\Delta v = 6.4 \text{ km s}^{-1}$) component. The redshifted wing of the broad component reported in Yamamoto et al. (1992) is weaker than the blueshifted wing, hence the redshifted wing was not detected probably due to the low signal-to-noise ratio in our observations.

4. DISCUSSION

4.1. CH₃OH and SiO Abundance

4.1.1. CH₃OH

The column density values of the CH₃OH molecule at the positions of the protostars were calculated by assuming the LTE condition using Equation (1). Since CH₃OH is not a linear molecule, the partition function was calculated from the energy level diagram (Xu & Lovas 1997). The excitation temperature was assumed to be 12 K, which is the same value as the kinetic temperature derived from NH₃ (Bachiller et al. 1990). We used the brightness temperature of the $2_{-1} - 1_{-1}$ E line in this calculation. Transitions between A and E species of CH₃OH are strictly prohibited, therefore the total column density of the CH₃OH molecule including both A and E species was estimated under the assumption that the abundance ratio between the A and E species is unity. The resulting column densities toward five YSOs are summarized in Table 5.

The fractional abundance values of the CH₃OH molecule at the protostellar positions were estimated by comparing the derived CH₃OH column densities with the H₂ column densities at the same positions. The H₂ column densities were calculated using the 850 μm dust continuum data observed with the JCMT SCUBA by the COMPLETE project (Ridge et al. 2006). Under the assumption of optically thin dust emission, the H₂ column density $N(\text{H}_2)$ is calculated by

$$N(\text{H}_2) = \frac{S_\nu^{\text{beam}}}{\Omega_{\text{beam}} \mu_{\text{H}_2} m_{\text{H}} \kappa_\nu B_\nu(T_{\text{D}})}, \quad (13)$$

where S_ν^{beam} is the flux density per beam, Ω_{beam} is the beam solid angle, κ_λ is the mass absorption coefficient per gram at 850 μm , and $B_\nu(T_{\text{D}})$ is the Planck function at a dust temperature T_{D} . We assume the dust temperature of 12 K and $\kappa_\lambda = 0.012 \text{ cm}^2 \text{ g}^{-1}$. The SCUBA image was smoothed to the 18'' resolution in order to match the beam size of the CH₃OH observations. The 850 μm flux densities, the derived column densities and abundance are summarized in Table 5.

The derived abundance ranges from 2.3×10^{-9} at SMM 1 to 9.4×10^{-9} at SMM 6, which

are in the same order of magnitude with the CH₃OH abundance in dark clouds, $2 - 5.1 \times 10^{-9}$ (Friberg et al. 1988; Dickens et al. 2000). The CH₃OH abundance values toward SMM 6 and SMM 11 are a few times larger than those toward the other SMM sources. These two sources with high CH₃OH abundance are accompanied both with the CO outflow shown in the present observations and the shock-excited IR emission (Walawender et al. 2005b). On the other hand, there was no shocked IR emission found around SMM 2 and no significant outflow signature in our CO (1 – 0) data toward SMM 1 and SMM 3. Therefore, the higher CH₃OH abundance values at SMM 6 and SMM 11 are considered to be influenced by the outflows. Such a variation of the CH₃OH abundance is also found toward other YSOs. The CH₃OH abundance was derived toward 30 Class 0 and Class I sources (Buckle & Fuller 2002), and the mean CH₃OH abundance was 1.9×10^{-8} for the sources with broad component whose FWHM is larger than 2.0 km s^{-1} , and was 4.8×10^{-9} for the sources without broad component. The CH₃OH abundance toward Class 0 sources is reported to be higher than that toward Class I sources (Buckle & Fuller 2002), however, our results show that the abundance depends on the presence of the broad line component rather than the evolutionary state of the sources.

Next, we examine the CH₃OH abundance in the outflow component around the position “a”. At the position “a”, the integrated intensity of the redshifted CH₃OH wing emission ($V_{\text{LSR}} > 9.6 \text{ km s}^{-1}$) is 1.1 K km s^{-1} . Under the assumption of the LTE condition with an excitation temperature of 50 K, which is same as that of the CO emission, the column density of the CH₃OH molecule was estimated to be $6.6 \times 10^{14} \text{ cm}^{-2}$. Since dust continuum emission at the position “a” is too faint to estimate the H₂ column density, we used the CO line intensity in the same velocity range as the CH₃OH emission to calculate the H₂ column density of the high velocity gas at this position. Under the assumption of the optically thin CO emission with an excitation temperature of 50 K, the CO column density was derived to be $1.8 \times 10^{16} \text{ cm}^{-2}$. The abundance ratio of CH₃OH to CO is $[\text{CH}_3\text{OH}/\text{CO}] = 3.6 \times 10^{-2}$, and comparable to the abundance ratio measured in other outflows (Garay et al. 2002). Assuming the CO abundance with respect to H₂ is 10^{-4} , the CH₃OH abundance ratio, $[\text{CH}_3\text{OH}/\text{H}_2]$, is 3.6×10^{-6} . This value is more than 2 orders of magnitude larger than the abundance toward the protostars in B1 and the abundance in dark clouds. It is obvious that the CH₃OH abundance is enhanced in the outflow.

4.1.2. SiO

The column density of the SiO molecule was estimated using Equation (1) under the LTE assumption. The rotation constant of the SiO molecule is 21,787 MHz (Lovas & Krupenie

1974) and the dipole moment of the SiO molecule is 3.1 D. We assumed the optically thin condition and adopted an excitation temperature of 50 K, the same assumption used to calculate the CO and CH₃OH column densities of the outflowing gas. Each SiO line profile was divided into the “high-velocity” and “low velocity” components in order to examine the difference of the abundance relative to CO in these two velocity ranges. The threshold of the two ranges was set to be $V_{\text{LSR}} = 9.6 \text{ km s}^{-1}$ following the velocity criterion used to separate the CO line core and wing component. The derived SiO column densities at five positions (SMM 2 W1, W2, W3, E, and SMM 6) are summarized in Table 6. The column density of the SiO molecule was derived to be $1 - 2 \times 10^{13} \text{ cm}^{-2}$ in the low-velocity component. The high velocity component was detected only at the positions of SMM 2 W2 and SMM 2 W3. The SiO column density in the high-velocity component of SMM 2 W3 was $5.4 \times 10^{13} \text{ cm}^{-2}$, which is a few times higher than the values measured in the low-velocity component. The relation between the total (high velocity + low velocity) SiO column density and the outflow velocity, which is determined from the terminal velocity of the SiO line, is shown in Fig. 8. The SiO column density tends to increase as the outflow velocity increases. Similar correlation between the SiO column density and the outflow velocity was also found in other protostellar outflows studied by Garay et al. (2002). These results support the idea that the more SiO molecules evaporate from dust grains into gas phase by collisions of the grains with higher velocity molecules in the outflows (Schilke et al. 1997). It should be noted that the SiO column density values reported in Garay et al. (2002) are 1 order of magnitude lower than those derived here. This is probably because the region covered by the telescope beam used by Garay et al. (2002) with HPBW of $57''$ was twice larger than that covered by our $38''.4$ beam. Since the size of the SiO emitting region is supposed to be smaller than the beams of the single-dish telescopes, the beam-averaged column density becomes lower if the source is observed with the larger beam. In addition, most of the sources in the sample of Garay et al. (2002) are located further away in distance.

The narrow (FWHM $\lesssim 1.0 \text{ km s}^{-1}$) SiO line as seen in SMM 6 was also detected in NGC 1333 (Lefloch et al. 1998; Codella et al. 1999), L1448-mm, and L1448 IRS3 (Jiménez-Serra et al. 2004). These authors proposed different mechanism for the SiO enhancement. Lefloch et al. (1998) and Codella et al. (1999) suggested that the emission is arisen from the postshock equilibrium gas after the interaction of protostellar jets with surrounding dense clumps. On the other hand, Jiménez-Serra et al. (2004) proposed that the emission is produced by the shock precursors associated with the protostellar jets. The narrow-line component around SMM 6 was detected only toward SMM 6 and does not have extended distribution like the one detected around NGC 1333 (Lefloch et al. 1998). The other difference is that the distribution of the narrow SiO line emission does not coincide with the high-velocity CO component in NGC 1333. These differences indicate that the mechanism to produce the

narrow SiO line emission is different in SMM 6 and NGC 1333 and it is likely that the shock precursor component produces the narrow line detected toward SMM 6.

The abundance of SiO relative to CO was estimated by comparing the column densities of these molecules. Since the beam size of the SiO observations is larger than that of the CO, the CO map was smoothed in order to match the angular resolution with the SiO. However, our CO map is undersampled, and does not recover the entire flux. Therefore, we assumed that the spatial distribution of the CO flux between the observed points varies smoothly, and interpolated the CO flux values at the missing points using the neighboring data. This smoothing makes the derived CO column density $\sim 25 - 40$ % smaller than the value without smoothing. The CO spectra in the “low velocity” range contain the emission from the quiescent ambient material that is unrelated with the outflows. Therefore in the calculation we adopted a method suggested by Margulis & Lada (1985) in which the line intensity originated from the low-velocity outflow is assumed to be the same as the line intensity at the boundary velocity between the line core and wing components; $V_{\text{LSR}} = 2.1$ km s $^{-1}$ and 9.6 km s $^{-1}$ for the blue- and redshifted outflow components, respectively. The CO integrated intensities in the low velocity range are estimated by assuming the uniform intensity over the integrated velocity range, 4.0 – 9.6 km s $^{-1}$ toward the positions along the SMM 2 outflow and 2.1 – 9.6 km s $^{-1}$ toward SMM 6. The integrated velocity range is defined to cover all the SiO emissions at each position. The derived SiO abundance values are summarized in Table 6. Assuming $[\text{CO}/\text{H}_2] = 10^{-4}$, the SiO abundance relative to H $_2$ is $10^{-7} - 10^{-8}$, 5–6 orders of magnitude higher than those measured in dark clouds ($< \text{a few } \times 10^{-12}$; Ziurys et al. 1989). The highest SiO/CO abundance of 4.7×10^{-3} was obtained in the high velocity component at SMM 2 W3. This abundance is 3 orders of magnitude higher than the abundance estimated toward several outflows (Garay et al. 2002) and comparable to the abundance at the extremely high-velocity (EHV) jet component in the L1448-mm outflow ($\sim 10^{-3}$; Bachiller et al. 1991). Such a high SiO abundance value and high terminal velocity (~ 50 km s $^{-1}$, corrected for the inclination angle of 57°3) suggest that the high-velocity SiO emission observed at SMM 2 W3 also arises from the jet component.

4.2. Outflows as an Engine of Interstellar Turbulence

Since protostellar outflows are considered to be the most likely mechanism to maintain the turbulent energy of the cloud (Li & Nakamura 2006), we examine the turbulent energy budget of B1 main core following the method described in Stanke & Williams (2007). The energy-loss rate due to the turbulence decay, L_{turb} , and the energy input rate by the outflows, L_{gain} , are compared.

According to numerical studies (Mac Low & Klessen 2004), the supersonic turbulence dissipates in a short period comparable to the free-fall timescale t_{ff} . Thus, L_{turb} is estimated by

$$L_{\text{turb}} = E_{\text{turb}}/t_{\text{ff}}, \quad (14)$$

where $E_{\text{turb}} = 3/2 M_{\text{core}} \sigma_{1\text{D}}^2$ is the energy of the turbulence, $\sigma_{1\text{D}}$ is the one-dimensional velocity dispersion. Since the observed region of the present study is well matched with the extent of B1 main core identified with the NH_3 observations (Bachiller et al. 1990), it is reasonable to adopt the mass M_{core} and the one-dimensional velocity dispersions $\sigma_{1\text{D}}$ of B1 main core ($65 M_{\odot}$ and 0.43 km s^{-1} ; Bachiller et al. 1990) in this calculation. The free-fall time t_{ff} is calculated to be $3.5 \times 10^5 \text{ yr}$ using a diameter of 0.5 pc and a mass of $65 M_{\odot}$. Therefore, the turbulence energy loss rate is calculated to be $L_{\text{turb}} = 8.5 \times 10^{-3} L_{\odot}$.

On the other hand, L_{gain} is calculated under the assumption that all the outflow momentum is transferred to the turbulent motion of the cloud,

$$L_{\text{gain}} = \frac{1}{2} \dot{M}_c \sigma_{3\text{D}}^2, \quad (15)$$

where $\dot{M}_c = F_{\text{outflow}}/\sigma_{3\text{D}}$ is the mass of the cloud which is accelerated up to the velocity $\sigma_{3\text{D}}$, F_{outflow} is the total momentum input rate by outflows, and $\sigma_{3\text{D}} = \sqrt{3}\sigma_{1\text{D}}$ is the three-dimensional velocity dispersion of the clump. The total momentum flux provided by the three outflows from SMM 2, SMM 6, and SMM 11 is $F_{\text{outflow}} = 1.8 \times 10^{-5} M_{\odot} \text{ km s}^{-1} \text{ yr}^{-1}$. Therefore, the energy input rate is calculated to be $L_{\text{gain}} = 1.1 \times 10^{-3} L_{\odot}$. This energy input rate is 1 order of magnitude smaller than the turbulence energy-loss rate.

There are some uncertainties in estimating the outflow energy input rate. The first issue is the effect of optical depth of the CO emission. Since our calculation assumed the optically thin CO wing emission, the energy input rate derived here is considered to be the lower limit. The mean opacity of the CO wing emission toward 16 YSOs is ~ 4 (Cabrit & Bertout 1992), and this value makes the energy input rate four times larger than that derived under the optically thin assumption. The second issue is the contribution of the low radial velocity component hidden in the line core. This effect becomes significant if the outflow axis is close to the plane of the sky, because most of the outflowing gas is moving along the transverse direction and shows the same radial velocity as the ambient gas. If the contribution of the "hidden" low radial velocity component is corrected by using the method described by Margulis & Lada (1985), which is also used to estimate the column density of the low-velocity outflow component in Section 4.1, the resulting energy input rate becomes twice as large as that calculated using the high-velocity wing component alone. The third issue is the contribution of the outflows that were not identified in the present observations. In addition

to the outflows from SMM 2, SMM 6, and SMM 11, other two outflows from SMM 1 and SMM 3 were identified in the CO (3 – 2) observations by Hatchell et al. (2007b). However, the contribution of these outflows to the total energy input is unlikely to be significant; the momentum flux value of the SMM 3 outflow is only $1.8 \times 10^{-7} M_{\odot} \text{ km s}^{-1} \text{ yr}^{-1}$ (Hatchell et al. 2007b), which are more than a factor of 20 smaller than that of the SMM 2 outflow. In addition, the redshifted component of the SMM 1 outflow is treated as a part of the outflows from SMM 2 and SMM11 in our calculations. In order to estimate the contribution of the weaker outflow components, we have integrated over all high-velocity component in the mapped area, and estimate the dynamical parameters of the high-velocity gas in this region. The total mass and momentum of the high velocity gas are derived to be $5.1 \times 10^{-2} M_{\odot}$ and $0.48 M_{\odot} \text{ km s}^{-1}$, respectively. If we assume that the dynamical timescale is $\sim 2 \times 10^4$ years, which is a typical timescale of the outflows in this region, the energy input rate is calculated to be $1.4 \times 10^{-3} L_{\odot}$. The energy input rate derived here is only a factor of 1.3 larger than that from SMM 2, SMM 6, and SMM 11 outflows, suggesting that most of the mechanical energy is supplied by the three major outflows. If we take the above issues into account, the outflow energy input rate can be 1 order of magnitude higher and becomes comparable to the turbulence energy decay rate. On the other hand, the efficiency of the energy transportation would be less than unity, because the extent of the outflow from SMM 2 and SMM 11 has already exceeded the dense part of the B1 main core region. Therefore, we conclude that the outflow energy input is not enough to maintain the turbulence in B1 main core. This result implies that the turbulence can not supply enough force against the gravity.

The magnetic field in B1 was measured by Crutcher et al. (1994) to be $30 \pm 4 \mu\text{G}$ and $16 \pm 3 \mu\text{G}$ in the NH_3 core ($r = 1.5$) and in the envelope ($r = 9'$), respectively, using OH Zeeman effect. The magnetic field strength, the size and the mean density of the NH_3 core in B1 are well reproduced by the magnetically supercritical, collapsing core (Crutcher et al. 1994). This result indicates that the magnetic field is not able to support the core. Since the mass-to-flux ratio (M/Φ) is independent of the distance to the object, the difference of the distances assumed in Crutcher et al. (1994) and the present study would not essentially affect the conclusion.

Since B1 is located in the Perseus cloud complex which contains several active star-forming regions, it is interesting to compare the star formation in B1 with that in other star-forming regions. Jørgensen et al. (2008) reported that there are eight protostars (i.e., Class 0 and Class I sources) out of nine YSOs in “B1 tight group”, which corresponds to the B1 main core region. Since the fraction of protostars (8/9) in B1 is higher than the other star forming regions in Perseus, such as NGC 1333 (35/102) and IC 348 (11/121), they suggested that the star formation activity in B1 has recently initiated. In order to compare the turbulent energy budget in B1 with that of the more evolved star forming region, we

have calculated the turbulence supply rate and decay rate of the NGC 1333 region. In the NGC 1333 region, six outflows were identified by the CO observations by Knee & Sandell (2000). The total momentum injection rate from these outflows is $\sim 5.6 \times 10^{-4} M_{\odot} \text{ km s}^{-1} \text{ yr}^{-1}$, which is ~ 30 times larger than that in B1. Using the velocity dispersion of 0.85 km s^{-1} , which is derived from the NH_3 observations (Schwartz et al. 1978), the energy input rate L_{gain} is estimated to be $6.8 \times 10^{-2} L_{\odot}$ in NGC 1333. On the other hand, if we adopt the mass of the core to be $319 M_{\odot}$, the turbulent decay rate L_{turb} is estimated to be $1.4 \times 10^{-1} L_{\odot}$. These two values agree within factor of 2, thus the outflows are powerful enough to maintain the turbulence in NGC 1333. Since Knee & Sandell (2000) assumed the lower excitation temperature of 20 K and did not apply the inclination correction, the energy input rate is underestimated compared to the case using our assumption of the excitation temperature of 50 K and the inclination angle of $57^{\circ}3$, in which the outflow momentum flux becomes a factor of 6 larger than the one originally derived by Knee & Sandell (2000). This makes the outflow energy input superior to the turbulence energy loss.

The magnetohydrodynamical simulation (Nakamura & Li 2007) shows that the cloud contraction proceeds in the initial phase of the cluster formation due to the decay of turbulence and decrease of the cloud momentum. This is consistent with the observed picture of B1 main core. The cloud reaches an equilibrium state in the later phase of the simulation because of the energy input by the outflows. As their simulations, when the outflows from the young Class 0 sources in B1 have enough evolved, it might be possible that the outflows have a considerable contribution to the energy balances of the turbulence.

5. SUMMARY

In order to study how outflows from protostars influence the physical and chemical conditions of the parent molecular cloud, we have observed B1 main core, which harbors four Class 0 and three Class I sources, in the CO ($J = 1 - 0$), CH_3OH ($J_K = 2_K - 1_K$), and the SiO ($J = 1 - 0$) lines using the NRO 45 m telescope. We have identified three CO outflows in this region; one is an elongated ($\sim 0.3 \text{ pc}$) bipolar outflow from a Class 0 protostar B1-c in the submillimeter clump SMM 2, another is a rather compact ($\sim 0.1 \text{ pc}$) outflow from a Class I protostar B1 IRS in the clump SMM 6, and the other is the extended outflow from SMM 11. No significant outflows from other YSOs were identified in our CO ($J = 1 - 0$) map. The CH_3OH emission lines are distributed around B1 main core with two peaks; one peak is located at the position of SMM 6, toward which the CH_3OH emission in the line core velocity ($5.5 < V_{\text{LSR}} < 7.5 \text{ km s}^{-1}$) is enhanced, and the other is $120''$ west of SMM 2, at the head of the redshifted CO lobe of the SMM 2 outflow, toward which the

CH₃OH line shows broad redshifted wing emission with a terminal velocity of 13 km s⁻¹. In the redshifted lobe of the SMM 2 outflow, the SiO line also shows broad redshifted wing whose terminal velocity reaches up to 25 km s⁻¹.

The CH₃OH and SiO abundances are significantly enhanced at the redshifted lobe of the SMM 2 outflow. It is likely that the shocks caused by the interaction between the outflow and ambient gas enhance the abundance of SiO and CH₃OH in the gas phase. Toward SMM 6, the CH₃OH and SiO lines are narrow and peak at the systemic velocity, however, the abundances of these molecules are enhanced compared with those in the quiescent dark clouds. Since the SiO emission around SMM 6 is localized at the position of the protostar, the origin of this narrow component is likely to be the shock precursor rather than the fossil outflow.

The turbulence energy decay rate and the outflow energy input rate are compared to investigate the energy budget in B1 main core. It is found that the energy input rate, $1.1 \times 10^{-3} L_{\odot}$, is approximately 1 order of magnitude smaller than the turbulence decay rate of $8.5 \times 10^{-3} L_{\odot}$. Even though several uncertainties that increase the energy input rate are taken into account, the outflows in B1 main core are not energetic enough to sustain the turbulence in this region. Since the magnetic field is not strong enough to prevent the gravitational collapse of B1 main core (Crutcher et al. 1994), it is likely that B1 main core is gravitationally unstable. The high fraction of protostars among YSOs (8/9) in B1 main core suggests that the star formation activity in this region has been started very recently. In the more evolved star-forming region, NGC 1333, the cloud can be supported by the turbulence driven by the outflows. These results are consistent with the picture of the cloud evolution proposed by Nakamura & Li (2007), in which molecular clouds contract due to the decay of turbulence in the early evolutionary phase, and become stable once the energy input from protostellar outflows become sufficient enough to balance the energy loss.

We are grateful to the NRO staff for supporting the telescope operation. Nobeyama Radio Observatory is a branch of the National Astronomical Observatory of Japan, National Institutes of Natural Sciences. This research has made use of the SIMBAD database, operated at CDS, Strasbourg, France.

Facilities: No:45m (BEARS)

REFERENCES

- Allamandola, L. J., Sandford, S. A., Tielens, A. G. G. M., & Herbst, T. M. 1992, *ApJ*, 399, 134
- Bachiller, R., Menten, K.M., & del Rio-Alvarez, S. 1990, *A&A*, 236, 461
- Bachiller, R., Martín-Pintado, J., & Fuente, A. 1991, *A&A*, 243, L21
- Bachiller, R. 1996, *ARA&A*, 34, 111
- Bachiller, R., Pérez Gutiérrez, M., Kumar, M. S. N., & Tafalla, M. 2001, *A&A*, 372, 899
- Bontemps, S., Andre P., Terebey, S., & Cabrit, S. 1996, *å*, 311, 858
- Borgman, J., & Blaauw, A. 1964, *Bull. Astron. Inst. Netherlands*, 17, 358
- Bourke, T. L., et al. 1997, *ApJ*, 476, 781
- Buckle, J. V. & Fuller, G. A. 2002, *A&A*, 381, 77
- Cabrit, S., & Bertout C. 1992, *A&A*, 261, 274
- Černis, K. & Straizys, V. 2003, *Baltic Astronomy*, 12,301
- Codella, C., Bachiller R., & Reipurth B. 1999, *A&A*, 343, 585
- Crutcher, R. M., Mouschovias, T. C., Troland, T. H., & Ciolek, G. E. 1994, *ApJ*, 427, 839
- de Zeeuw, P. T., Hoogerwerf, R., de Bruijne, J. H. J., Brown, A. G. A., & Blaauw, A. 1999, *AJ*, 117, 354
- de Gregorio-Monsalvo, I., Chandler, C. J., Gómez, J. F., Kuiper, T. B. H., Torrelles, J. M., & Anglada, G. 2005, *ApJ*, 628, 789
- Dickens, J. E., Irvine, W. M., Snell, R. L., Bergin, E. A., Schloerb, F. P., Pratap, P., & Miralles, M. P. 2000, *ApJ*, 542, 870
- Friberg, P., Madden, S. C., Hjalmarsen, Å, & Irvine, W. M. 1988, *A&A*, 195, 281
- Garay, G., Mardones, D., Rodríguez, L. F., Caselli, P., & Bourke, T. L. 2002, *ApJ*, 567, 980
- Giovanardi, C., Lizano, S., Natta, A., Evans, N. J., II, & Heiles, C. 1992, *ApJ*, 397, 214
- Hatchell, J., Fuller, G. A., Richer, J. S., Harries, T.J.,& Ladd, E. F. 2007 *A&A*, 468, 1009

- Hatchell, J., Fuller, G. A., & Richer, J. S. 2007, *A&A*, 472, 187
- Hirano, N., Kameya, O., Mikami, H., Saito, S., Umemoto, T., & Yamamoto, S. 1997, *ApJ*, 478, 631
- Hirano, N., Kamazaki, T., Mikami, H., Ohashi, N., & Umemoto, T. 1999, *Star Formation 1999, Proceedings of Star Formation 1999*, ed. T. Nakamoto, Nobeyama Radio Observatory, 181
- Hirota T., et al. 2008, *PASJ*, 60, 37
- Jiménez-Serra, I., Martín-Pintado, J., & Rodríguez-Franco, A. 2004, *ApJ*, 604, L49
- Jørgensen, J. K., Hogerheijde, M. R., Blake, G. A., van Dishoeck, E. F., Mundy, L. G., & Shöier, F. L. 2004, *A&A*, 415, 1021
- Jørgensen, J. K., et al. 2006, *ApJ*, 645, 1246
- Jørgensen, J. K., Johnstone, D., Kirk, H., Myers, P. C., Allen, L. E., & Shirley, Y. L. 2008, *ApJ*, 683, 822
- Knee, L. B. G. & Sandell, G. 2000, *A&A*, 361, 671
- Kutner, M., & Ulich, B. L. 1981, *ApJ*, 250, 341
- Lefloch, B., Castets, A., Cernicharo, J., & Leinard, L. 1998, *ApJ*, 504, L109
- Li, Z. Y., & Nakamura, F. 2006, *ApJ*, 640, L187
- Lovas, F. J., & Krupenie, P. H. 1974, *J. Phys. Chem. Ref. Data*, 3, 245
- Mac Low, M.-M., Klessen, R. S., Andreas, B., & Smith, M. D. 1998, *Phys. Rev. Lett.*, 80, 2754
- Mac Low, M.-M., & Klessen, R. S. 2004, *Rev. Mod. Phys.*, 76, 125
- Margulis, M., & Lada, C. J. 1985, *ApJ*, 299, 925
- Matthews, B. C., & Wilson, C. D. 2002, *ApJ*, 574, 822
- Matthews, B. C., Hogerheijde, M. R., Jørgensen, J. K., & Bergin, E. A. 2006, *ApJ*, 652, 1374
- Müller, H. S. P., Thorwirth, S., Roth, D. A., & Winnewisser, G. 2001, *A&A*, 370, L49
- Nakamura, F., & Li, Z. Y. 2007, *ApJ*, 662, 395

- Norman, C., & Silk, J. 1980, ApJ, 238, 158
- Ridge, N., et al. 2006, ApJ, 131, 2921
- Schilke, P., Walmsley, C. M., Pineau des Forêts, G., & Flower, D. R. 1997, A&A, 321, 293
- Schwartz, P. R., Bologna, J. M., & Waak, J. A. 1978, ApJ, 226, 469
- Stanke, T., & Williams, J. P. 2007, AJ, 133, 1307
- Sunada, K., Yamaguchi, C., Nakai, N., Sorai, K., Okumura, S. K., and Ukita, N. 2000, Proc. SPIE, 4015, 237
- Walawender, J., Bally, J., & Reipurth, B. 2005, AJ, 129, 2308
- Walawender, J., Bally, J., Kirk, H., & Johnstone, D. 2005, AJ, 130, 1795
- Walawender, J., Reipurth, B., & Bally, J. 2009, AJ, 137, 3254
- Xu, L.-H., & Lovas, F. J. 1997, J. Phys. Chem. Ref. Data, 26, 17
- Yamamoto, S., Mikami, H., Saito, S., Kaifu, N., Ohishi, M., & Kawaguchi, K. 1992, PASJ, 44, 459
- Ziurys, L. M., Friberg, P. & Irvine, W. M. 1989, ApJ, 343, 201

Table 1. Young Stellar Objects in B1

Name	α (J2000)	δ (J2000)	L_{bol} (L_{\odot})	T_{bol} (K)	Class	other names
SMM 1	03 33 21.5	31 07 29	<2.5	<25	0	B1-bN and B1-bS
SMM 2	03 33 18.0	31 09 32	3.7	53	0	B1-c
SMM 3	03 33 16.3	31 06 53	2.6	32	0	B1-d
SMM 6	03 33 16.6	31 07 47	1.3	158	I	B1-a, B1 IRS, IRAS 03301+3057
SMM 11	03 33 27.3	31 07 08	0.4	117	I	
LkH α 327	03 33 30.4	31 10 51			I	IRAS 03304+3100

Note. — Positions of the SMM sources are referred from Walawender et al. (2005b), and that of LkH α 327 is obtained from Simbad. L_{bol} , T_{bol} , and Class of the SMM sources are referred from Hatchell et al. (2007a). The class of LkH α 327 is from Walawender et al. (2005b).

Table 2. Observed Molecular Lines

Molecule	Transition	Frequency (GHz)	E_u (K)
CO	$J = 1 - 0$	115.2712	5.53
CH ₃ OH	$J_K = 2_{-1} - 1_{-1} E$	96.73939	4.64
	$J_K = 2_0 - 1_0 A^+$	96.74142	6.79
	$J_K = 2_0 - 1_0 E$	96.74458	12.2
SiO	$J = 1 - 0$	43.42386	2.08

Note. — The upper state energies of the CH₃OH E and A^+ symmetric state are the values relative to the ground state of $1_{-1} E$ and $0_0 A^+$, respectively. The $1_{-1} E$ level is 7.9 K above the $0_0 A^+$ level.

Table 3. CO Line Intensity Ratio

Source	Position (CO 3 – 2)		Integ. Vel. Range (km s ⁻¹)	$\int T_{\text{MB},3-2} dv$ (K km s ⁻¹)	$\int T_{\text{MB},1-0} dv$ (K km s ⁻¹)	T_{ex} (K)
	α (J2000)	δ (J2000)				
SMM 2 red	03 33 15.866	31 09 49.13	10 – 20	24.8	4.5	46
SMM 6	03 33 16.257	31 07 49.13	–10 – 2	33.2	6.2	42

Table 4. Outflow Parameters

Component	M (M_{\odot})	P ($M_{\odot}\text{km s}^{-1}$)	\dot{M} ($M_{\odot}\text{yr}^{-1}$)	t_{d} (yr)	E_{k} ($M_{\odot}\text{km}^2\text{s}^{-2}$)	F ($M_{\odot}\text{km s}^{-1}\text{yr}^{-1}$)
SMM 2						
Blue	1.5×10^{-2}	0.14	4.8×10^{-8}	2.9×10^4	0.66	4.8×10^{-6}
Red West	5.3×10^{-3}	3.9×10^{-2}	1.8×10^{-8}	2.1×10^4	0.17	1.8×10^{-6}
Red East	5.2×10^{-3}	3.3×10^{-2}	2.1×10^{-8}	1.6×10^4	0.11	2.1×10^{-6}
Total	2.5×10^{-2}	0.21	8.7×10^{-8}		0.93	8.7×10^{-6}
SMM 6						
Blue	1.2×10^{-3}	1.2×10^{-2}	1.1×10^{-8}	1.1×10^4	5.6×10^{-2}	1.1×10^{-6}
Red	2.3×10^{-3}	1.7×10^{-2}	9.8×10^{-9}	1.8×10^4	7.0×10^{-2}	9.8×10^{-7}
Total	3.5×10^{-3}	2.9×10^{-2}	2.0×10^{-8}		0.13	2.0×10^{-6}
SMM 11						
Blue	1.4×10^{-2}	0.14	6.1×10^{-8}	2.3×10^4	0.72	6.1×10^{-6}
Red	5.1×10^{-3}	3.0×10^{-2}	9.4×10^{-9}	3.2×10^4	8.7×10^{-2}	9.4×10^{-7}
Total	1.9×10^{-2}	0.17	7.0×10^{-8}		0.81	7.0×10^{-6}

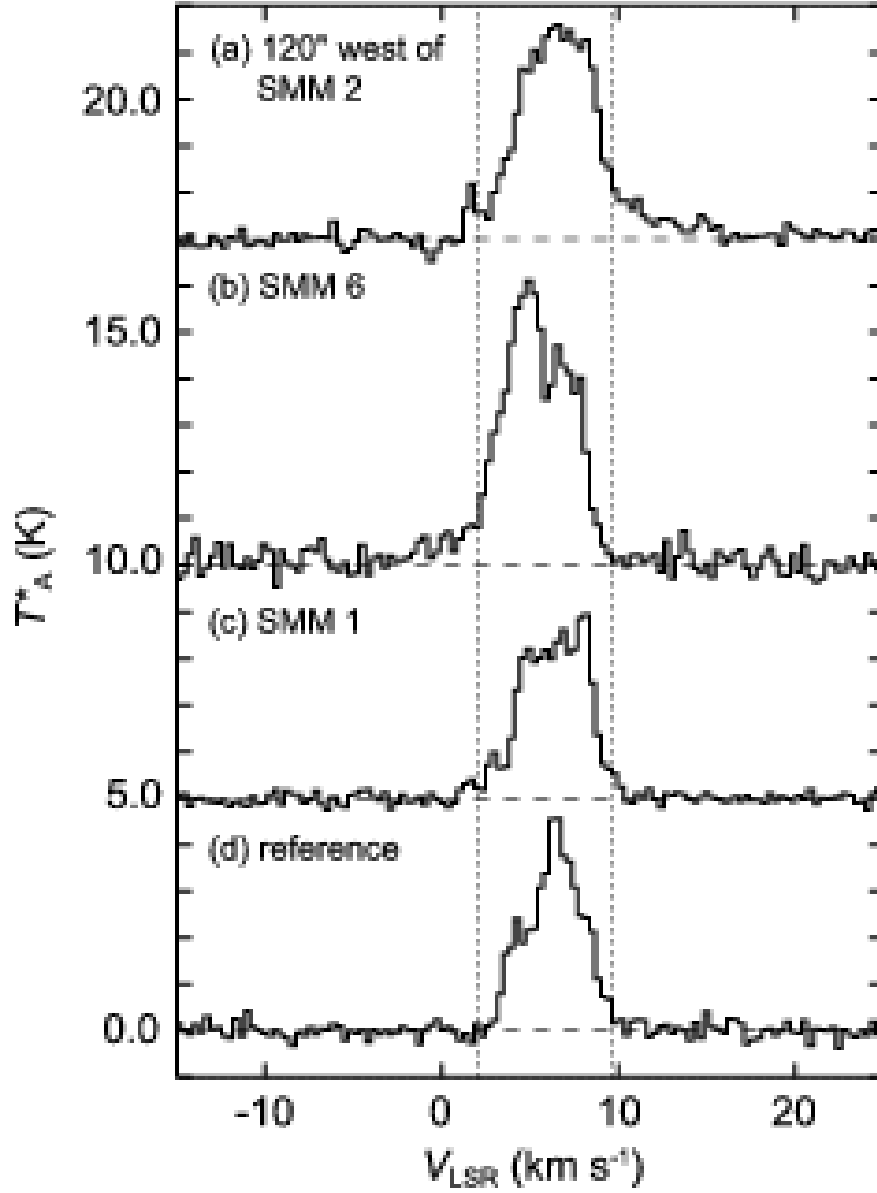


Fig. 1.— CO ($J = 1 - 0$) line profiles toward (a) $120''$ west of SMM 2, (b) SMM 6, (c) SMM 1 and (d) $5'.5$ southwest of SMM 6. The velocity resolution is 0.3 km s^{-1} . Vertical lines indicate the outflow velocity boundaries.

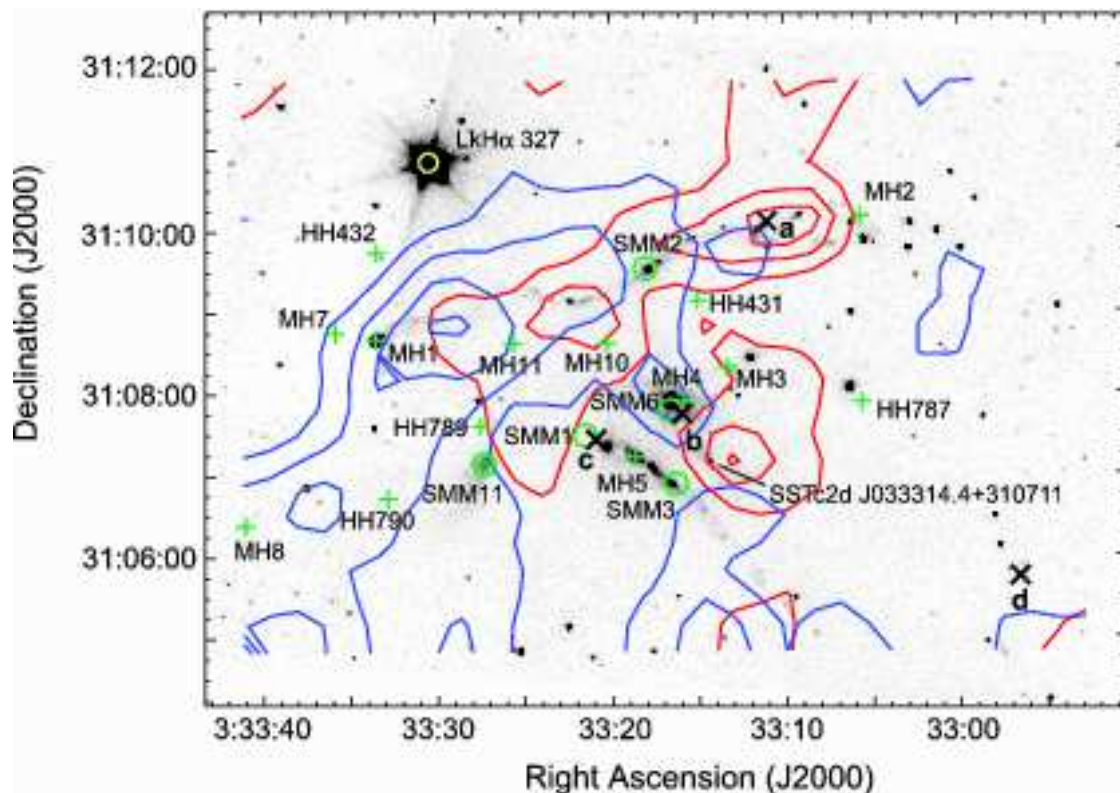


Fig. 2.— Distribution of the high velocity component of the CO ($J = 1 - 0$) line. The blueshifted ($-8.1 \text{ km s}^{-1} \leq V_{\text{LSR}} \leq +2.1 \text{ km s}^{-1}$) and the redshifted ($9.6 \text{ km s}^{-1} \leq V_{\text{LSR}} \leq 19.8 \text{ km s}^{-1}$) components are drawn with blue and red contours, respectively. The first contour level and the contour interval are 3σ , which correspond to 0.5 K km s^{-1} for blue and 0.68 K km s^{-1} for red contours, respectively. The gray-scale image in the background is the *Spitzer* IRAC2 $4.5 \mu\text{m}$ image. Circle and cross marks indicate the positions of protostars and H_2 knots (Walawender et al. 2005b), respectively. X marks indicate the positions “a” to “d” in Fig.1.

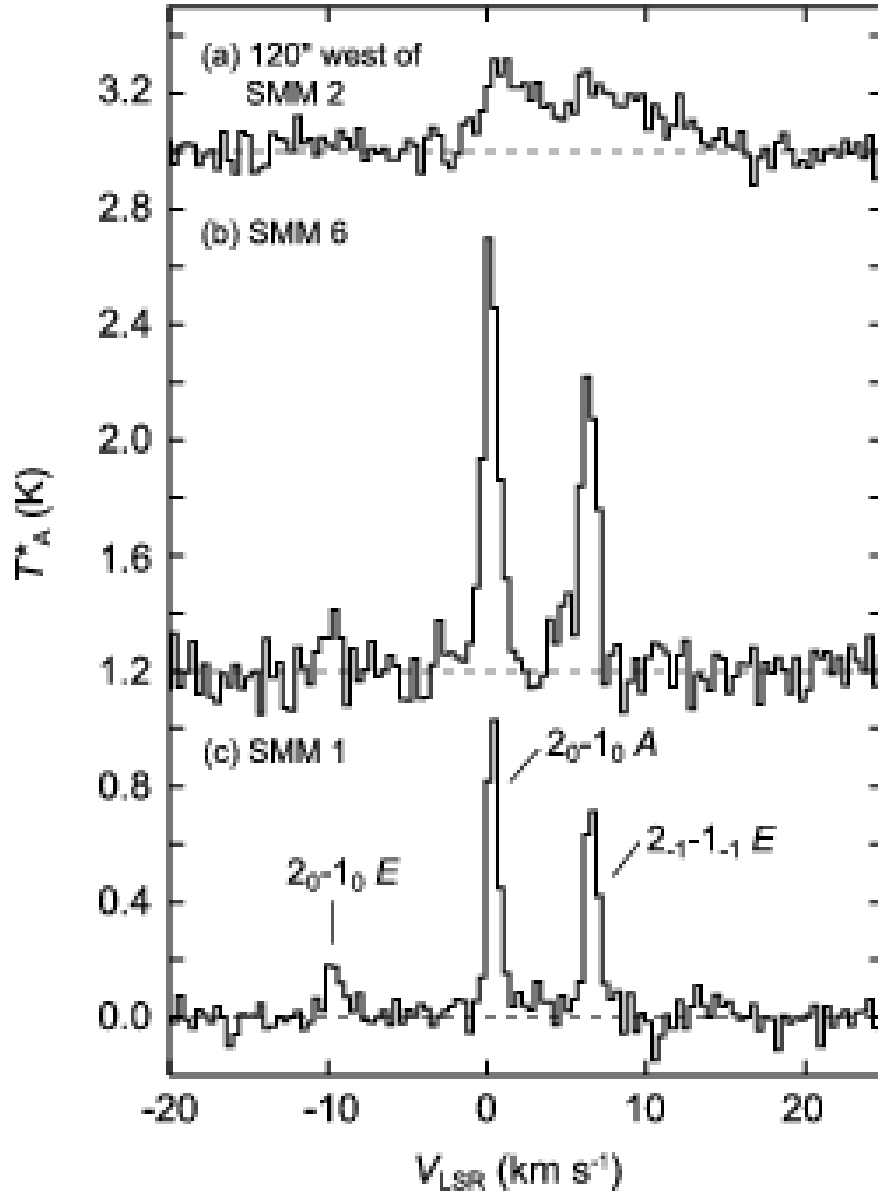


Fig. 3.— CH_3OH ($J_K = 2_0 - 1_0 E$, $= 2_0 - 1_0 A$, and $2_{-1} - 1_{-1} E$) line profiles toward (a) 120" west of SMM 2, (b) SMM 6, and (c) SMM 1. The velocity resolution is 0.3 km s^{-1} . The reference frequency in the velocity calculation is set to be 96.73939 GHz, the rest frequency of $2_{-1} - 1_{-1} E$ transition.

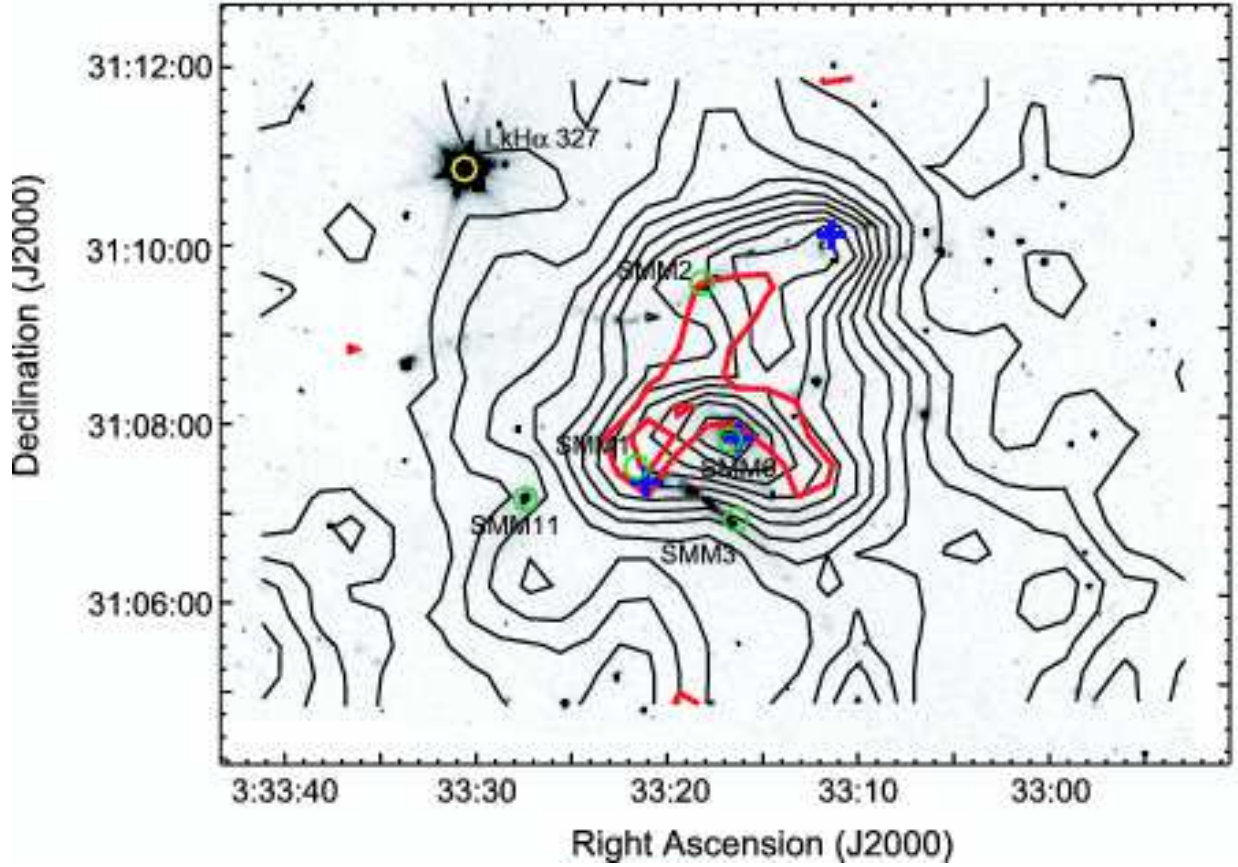


Fig. 4.— Integrated intensity map of the CH₃OH lines. Black contours represent the integrated intensity of the $J_K = 2_{-1} - 1_{-1} E$ and $2_0 - 1_0 A^+$ lines ($A + E$ map). Red contours show the integrated intensity of the $2_0 - 1_0 E$ line. Both the lowest contour level and the interval are 0.23 K km s^{-1} (6σ) for the $A + E$ map. The lowest contour level is 0.13 K km s^{-1} and the contour interval is $0.043 \text{ K km s}^{-1}$ (1σ noise level) for the $2_0 - 1_0 E$ line. The integrated velocity range is $-3.6 < V_{\text{LSR}} < 20.4 \text{ km s}^{-1}$ for the $A + E$ map and $2.9 < V_{\text{LSR}} < 10.2 \text{ km s}^{-1}$ for the $2_0 - 1_0 E$ line. The position “a” and the protostars are marked with a cross and circles.

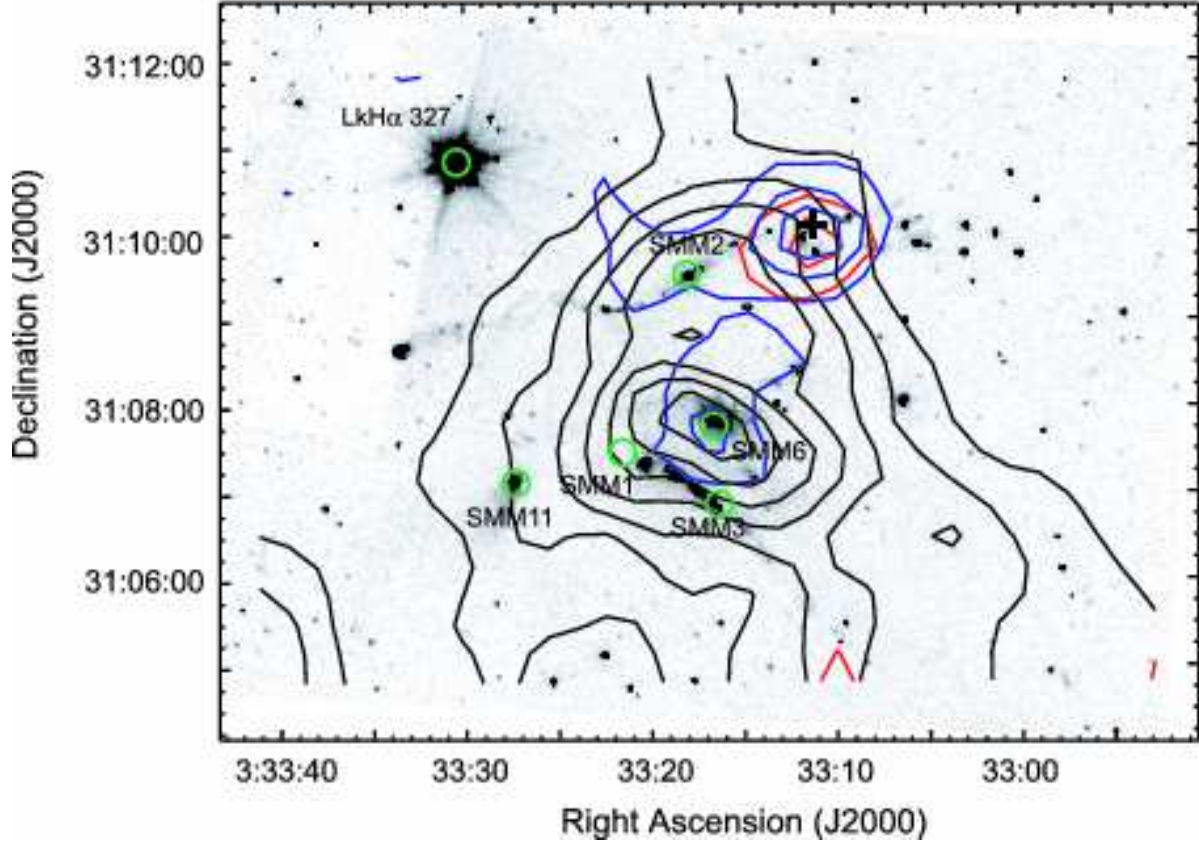


Fig. 5.— Integrated intensity map of the CH_3OH ($J_K = 2_{-1} - 1_{-1} E$) line in the line core velocity range ($5.5 \text{ km s}^{-1} < V_{\text{LSR}} < 7.5 \text{ km s}^{-1}$, black contours) and the higher velocity range ($2.5 \text{ km s}^{-1} < V_{\text{LSR}} < 5.5 \text{ km s}^{-1}$ in blue contours and $7.5 \text{ km s}^{-1} < V_{\text{LSR}} < 20 \text{ km s}^{-1}$ in red contours). Note that the blueshifted component around the position “a” (black cross) is due to a contamination of redshifted emission of the $J_K = 2_0 - 1_0 A^+$ line. The lowest contour and contour intervals are 3σ noise level of each map, 0.12 K km s^{-1} for the line core, 0.09 K km s^{-1} for the blueshifted, and 0.24 K km s^{-1} for the redshifted component.

Table 5. CH₃OH Column Density and Abundance

Source	$\int T_{\text{MB}} dv$ (K km s ⁻¹)	N (cm ⁻²)	$S_{850\mu\text{m}}$ (Jy beam ⁻¹)	$N(\text{H}_2)$ (cm ⁻²)	[CH ₃ OH/H ₂]	Shocked IR
SMM 1	1.9	2.3×10^{14}	1.0	1.0×10^{23}	2.3×10^{-9}	No
SMM 2	1.7	2.0×10^{14}	0.87	8.6×10^{22}	2.4×10^{-9}	No
SMM 3	1.3	1.6×10^{14}	0.64	6.3×10^{22}	2.5×10^{-9}	Yes
SMM 6	3.4	4.1×10^{14}	0.44	4.4×10^{22}	9.4×10^{-9}	Yes
SMM 11	0.58	7.1×10^{13}	0.12	1.1×10^{22}	6.2×10^{-9}	Yes

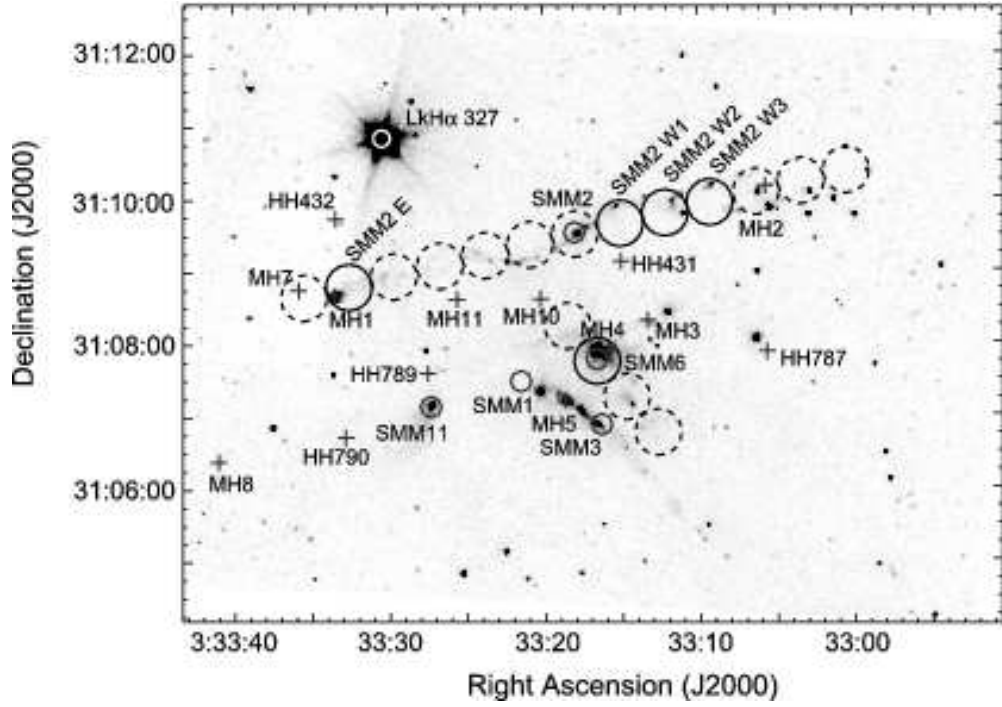


Fig. 6.— SiO ($J = 1-0$) observing positions overlaid on the *Spitzer* IRAC2 image. The large circles with solid and broken lines indicate the positions where the SiO line was detected and not detected, respectively. The size of the circles corresponds to the HPBW in the frequency of the line (43.4 GHz).

Table 6. SiO Column Density Along the Outflows

Source	α (J2000)	δ (J2000)	High Velocity			Low Velocity		
			$\int T_{\text{MB,SiO}} dv$ (K km s ⁻¹)	$N(\text{SiO})$ (cm ⁻²)	[SiO/CO]	$\int T_{\text{MB,SiO}} dv$ (K km s ⁻¹)	$N(\text{SiO})$ (cm ⁻²)	[SiO/CO]
SMM 2 W3	3 33 09.3	31 09 57.9	2.6	5.4×10^{13}	4.7×10^{-3}	0.78	1.6×10^{13}	9.1×10^{-4}
SMM 2 W2	3 33 12.2	31 09 49.2	0.69	1.4×10^{13}	1.4×10^{-3}	0.83	1.7×10^{13}	1.0×10^{-3}
SMM 2 W1	3 33 15.1	31 09 40.6	0.47	9.8×10^{12}	5.1×10^{-4}
SMM 2 E	3 33 29.7	31 08 57.4	0.59	1.2×10^{13}	2.7×10^{-4}
SMM 6	3 33 16.6	31 07 46.8	1.1	2.3×10^{13}	2.1×10^{-3}

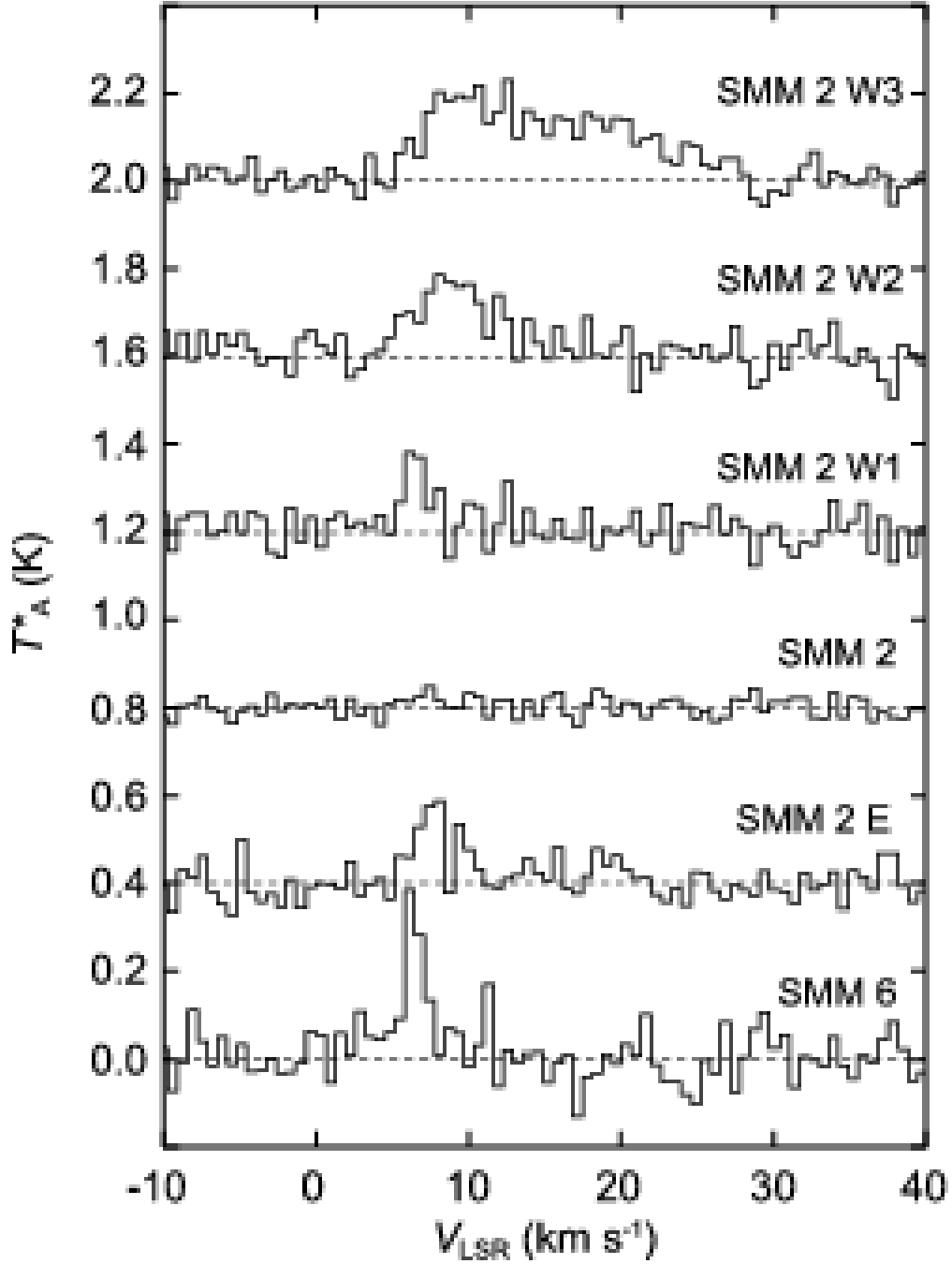


Fig. 7.— SiO ($J = 1 - 0$) line profiles along the outflow axis of SMM 2 and at the position of SMM 6. The velocity resolution is 0.5 km s^{-1} .

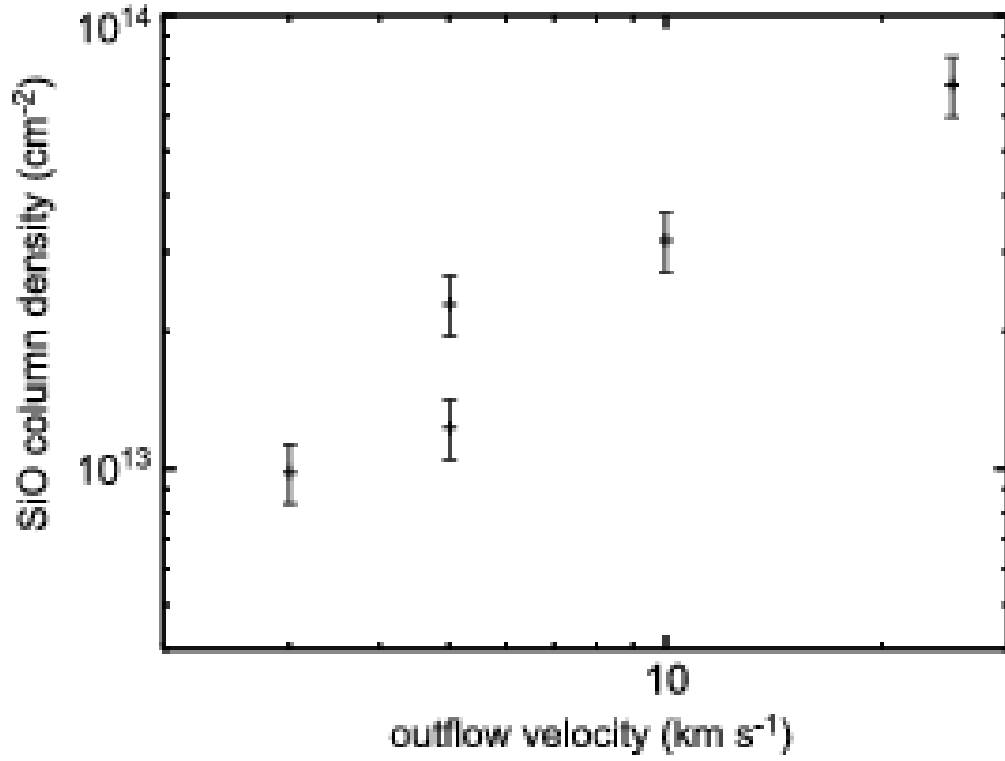


Fig. 8.— Relation between the outflow terminal velocity measured from the systemic velocity at each point and the column density of the SiO molecule. The errors are calculated from the absolute intensity calibration uncertainty ($\sim 15\%$).